How to cite: *Angew. Chem. Int. Ed.* **2021**, *60*, 19829–19835
International Edition: doi.org/10.1002/anie.202105343
German Edition: doi.org/10.1002/ange.202105343

Electrocatalytic CO_2RR

Partial Coordination-Perturbed Bi-Copper Sites for Selective Electroreduction of CO_2 to Hydrocarbons

Rui Wang, Jiang Liu, Qing Huang, Long-Zhang Dong, Shun-Li Li, and Ya-Qian Lan**

Abstract: *In the electrochemical CO_2 reduction reaction (CO_2RR), it is challenging to develop a stable, well-defined catalyst model system that is able to examine the influence of the synergistic effect between adjacent catalytic active sites on the selective generation of C1 or C2 products. We have designed and synthesized a stable crystalline single-chain catalyst model system for electrochemical CO_2RR, which involves four homomorphic one-dimensional chain-like compounds (**Cu-PzH**, **Cu-PzCl**, **Cu-PzBr**, and **Cu-PzI**). The main structural difference of these four chains is the substituents of halogen atoms with different electronegativity on the Pz ligands. Consequently, different synergistic effects between bi-copper centers lead to changes in the faradic efficiency (FE_{CH_4}:$FE_{C_2H_4}$). This work provides a simple and stable crystalline single-chain model system for systematically studying the influence of coordination microenvironment on catalytically active centers in the CO_2RR.*

Introduction

Electrocatalytic CO_2 reduction reaction (CO_2RR) is an important green conversion pathway that can convert CO_2 into value-added C-based energy chemicals for reuse.[1] It is widely believed that selectively convert CO_2 into C1 or C2 hydrocarbon reduction products with high combustion value and energy density is a desirable choice, such as methane (CH_4) and ethylene (C_2H_4).[2] In order to effectively regulate the selectivity of specific hydrocarbon reduction products, it is generally considered that constructing a well-designed catalyst structure plays a crucial role in clearly understanding the structure-performance relationship and electrocatalytic reaction mechanism.[3] At present, Cu-based nanomaterials/nanocomposites are widely treated as the most effective electrocatalysts for CO_2RR in literature, because they are capable of selectively reducing CO_2 into different hydrocarbon products.[4] Especially in flow cell with a gas diffusion layer (GDL), the three-phase interface (alkaline electrolyte/catalyst/CO_2) can overcome the mass transfer limit of CO_2 and solve the problem of the low solubility of CO_2;[5] the alkaline environment can effectively inhibit HER and reduce the activation energy barrier of C–C coupling.[6] Currently, a variety of high-performance Cu-based catalyst materials have been designed and synthesized to study the electrocatalytic reaction mechanisms of CO_2-to-hydrocarbon conversions by adjusting the crystal facets/phases,[7] material composition,[8] size effect,[9] morphology,[10] metal alloys,[11] valence state,[12] doping,[13] etc. However, investigating the influence of the synergistic effect between adjacent catalytic active sites derived from the coordination microenvironment variation on the selective generation of C1 or C2 products is rarely reported.

In the process of CO_2RR, the variation of the direct coordination microenvironment of catalytic active center usually has an important impact on its charge density distribution and structural geometry, which may lead to significant free energy changes of different intermediate species adsorbed on the catalytic site, and then affect the activation path and selectivity of the specific hydrocarbon product.[14] Especially for the formation of multi-carbon products, it often requires the synergistic effect of adjacent catalytic active sites where the change of structural geometry (such as distance and angle) is likely to influence the probability of C–C coupling greatly. In this case, establishing a well-defined catalyst model system to intuitively understand the impact of the coordination microenvironment's changes on the selectivity and conversion mechanism of hydrocarbon products is very important and necessary.[15] Crystalline electrocatalyst materials with clear crystallographic information and structural designability are expected to be ideal catalyst models for satisfying the abovementioned conditions; because they can provide a nearly visual research platform to identify the real catalytic active sites and monitor the change of coordination structure geometry.[16] Moreover, their clear crystal structures can offer accurately theoretical calculation models to study the impacts of the synergistic effect caused by the coordination microenvironment of adjacent catalytic active sites on electrocatalytic reaction mechanism and selectivity of the specific hydrocarbon products. However, the challenge for limiting crystalline materials applied to flow cell is always their structural instability, and thus only a few stable crystal materials are competent to this reaction to date. In addition, although many electrocatalysts modified by halogen show relatively good catalytic performance,[17] there is currently no report in the literature that adjusting the second coordination environment by using halogens can affect the synergistic effect between two adjacent catalytically active sites and ultimately lead to different product selectivities.

[*] Dr. R. Wang, Prof. J. Liu, Dr. L.-Z. Dong, Prof. S.-L. Li, Prof. Y.-Q. Lan
Jiangsu Key Laboratory of Biofunctional Materials, School of Chemistry and Materials Science, Nanjing Normal University
Nanjing 210023 (P. R. China)
E-mail: liuj@njnu.edu.cn
yqlan@njnu.edu.cn
Prof. J. Liu, Dr. Q. Huang, Prof. S.-L. Li, Prof. Y.-Q. Lan
School of Chemistry, South China Normal University
Guangzhou, 510006 (P. R. China)
Supporting information and the ORCID identification number(s) for the author(s) of this article can be found under: https://doi.org/10.1002/anie.202105343.

Based on the above considerations, we elaborately design and synthesize a series of stable homomorphic one-dimensional (1D) chain compounds, $[Cu(4\text{-}XPz)_2]_n$·solvent, (X = H, Cl, Br, I; Pz = pyrazole), named as **Cu-PzH**, **Cu-PzCl**, **Cu-PzBr**, and **Cu-PzI**, respectively. The main difference among these chain structures is the substituents of halogen atoms with different electronegativity on the Pz ligands coordinated to crystallographic dependent Cu atom, which results in the distance ($D_{Cu\text{-}Cu}$) and dihedral angle ($\beta_{Cu\text{-}Cu}$) variations of contiguous active Cu sites within the chains. Therefore, these crystalline single chains can serve as a model electrocatalyst system to study the influence of coordination microenvironmental variation of neighboring catalytic active sites on the selectivity and electrocatalytic reaction mechanism of CO_2RR. Furthermore, these crystalline chains are stable in strongly alkaline solution (pH 14) for more than three days and maintain the integrity of the structures, which are believed to be the potential crystalline electrocatalysts for CO_2RR in flow cell. In these chain structures, the variations of coordination microenvironment induce the different synergistic effects: the change of $D_{Cu\text{-}Cu}$ (from 3.57 to 3.63 Å) and $\beta_{Cu\text{-}Cu}$ (from 74.48 to 70.87°) between bi-Cu centers, directly leading to the regular ratio FE_{CH_4} : $FE_{C_2H_4}$ changes from 1:6.5, 1:2.3, 1:1.2 to 1:0.3 (Scheme 1). At −1.0 V (vs. RHE), the $FE_{C_2H_4}$ of **Cu-PzH** reaches up to 60% with a larger current density (−346.46 mA cm^{-2}), which is the highest in Cu-based crystalline materials. In contrast, **Cu-PzI** exhibits the highest FE_{CH_4} of 52% with the partial current density (−287.52 mA cm^{-2}). Based on accurate crystalline structure models, density functional theory (DFT) calculations discover that **Cu-PzH** ($D_{Cu\text{-}Cu}$ = 3.57 Å, $\beta_{Cu\text{-}Cu}$ = 74.48°) has the lowest reaction energy barrier for C_2H_4 generation because of the shortest *CO···*COH distance (1.483 Å) for C–C coupling. In contrast, **Cu-PzI** ($D_{Cu\text{-}Cu}$ = 3.63 Å, $\beta_{Cu\text{-}Cu}$ = 70.87°) is more inclined to the protonation of *CO to produce CH_4 with the lowest reaction energy barrier. It can be concluded that coordination microenvironment variations obviously affect the changes of the synergistic effect of neighboring bi-copper centers and the *d*-band center, and then regulate the adsorption ability of the key intermediate species (*COCOH and *HCO). This work provides a simple and stable crystalline model system for systematically and intuitively studying the important influence of the slight variations of the synergistic effect of adjacent catalytic active sites on the electroreduction of CO_2 to C1 or C2 products.

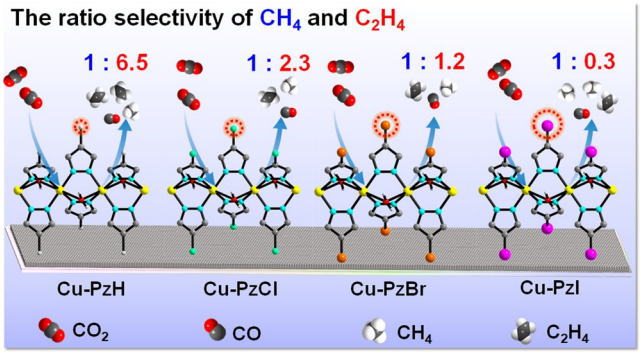

Scheme 1. Illustration of the difference in selectivity for Cu-PzX (where X = H, Cl, Br, I) in the electrochemical CO_2RR.

Results and Discussion

Single crystal X-ray diffraction studies reveal that **Cu-PzH** crystallizes in orthorhombic with a space group *Cmcm*,[18] while **Cu-PzCl**, **Cu-PzBr**, **Cu-PzI** crystallize in monoclinic $P2_1/m$ space group (Supporting Information, Table S1). The main bodies of these four compounds are one-dimensional chain-like structures. In these chains, the asymmetric unit has only one crystallographically independent Cu1 atom, whose coordination environment is octahedral geometry. Cu_1 atom is connected with four nitrogen atoms of four ligands on the equatorial plane, and coordinates two water molecules on the axial position, which are easy to leave under external stimulation. The coordination environment of neighboring bi-Cu atoms within every chain structure is the same. The more detailed structural information of the four chains is shown in Figures S1–S4 (Supporting Information). Moreover, the main structural difference of these four chains is the variations of coordination microenvironment of Cu1 atom, which refers to the 4-position of pyrazole (4-XPz) is occupied by different electronegative atoms (X = H, Cl, Br, I) on the equatorial plane (Figure 1a). With the variations of coordination microenvironment, the distance ($D_{Cu\text{-}Cu}$) between adjacent bi-Cu sites changes (3.64 Å for **Cu-PzH**, 3.61 Å for **Cu-PzCl**, 3.60 Å for **Cu-PzBr**, and 3.64 Å for **Cu-PzI**) in the overall structure, and so is the dihedral angle ($\beta_{Cu\text{-}Cu}$), which is defined by the intersection of two equatorial planes of

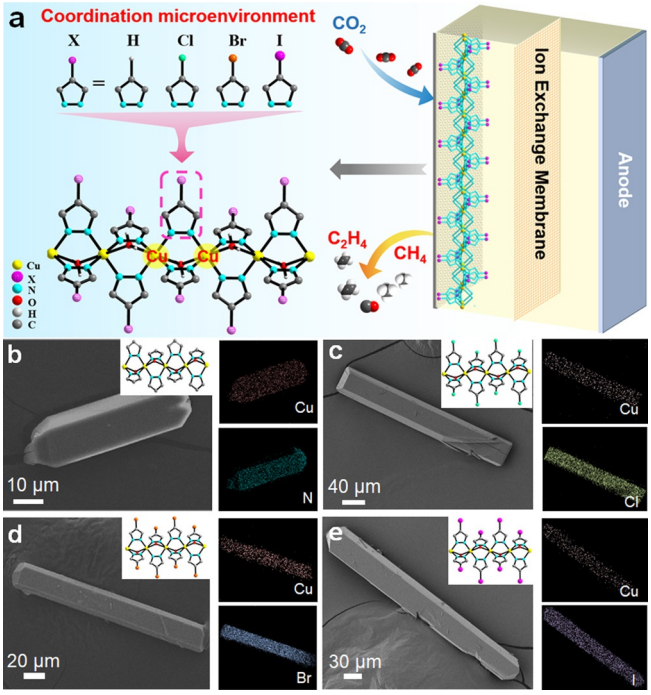

Figure 1. The structure and characterization of Cu-PzX (where X = H, Cl, Br, I). a) The chain structures of Cu-PzX catalysts used for electrochemical CO_2RR in a flow cell. b–e) STEM and mapping images of **Cu-PzX** (b), **Cu-PzH** (c), **Cu-PzCl** (d), **Cu-PzBr**, and **Cu-PzI** (e).

neighboring Cu1 atoms. The dihedral angles ($\beta_{Cu\text{-}Cu}$) of **Cu-PzH**, **Cu-PzCl**, **Cu-PzBr**, **Cu-PzI** are 71.67°, 73.27°, 72.51°, and 70.30°, respectively. It is worth noting that the axial water molecules of the Cu atom are easy to leave to become active sites for the adsorption and activation of small molecules (e.g., CO_2). Of course, the distance ($D_{Cu\text{-}Cu}$) and dihedral angle($\beta_{Cu\text{-}Cu}$) between adjacent bi-copper atoms also change with the departure of coordination water molecules: the distances ($D_{Cu\text{-}Cu}$) for **Cu-PzH**, **Cu-PzCl**, **Cu-PzBr**, and **Cu-PzI** gradually increase from 3.57 Å, 3.60 Å, 3.61 Å to 3.63 Å, but dihedral angles ($\beta_{Cu\text{-}Cu}$) decrease from 74.48°, 72.42°, 71.82° to 70.87°. Finally, these four single chains are all further stacked through intermolecular interactions to form three-dimensional supramolecular structures.

The powder X-ray diffraction (PXRD) proves that the experimental peaks of **Cu-PzX** are consistent with their simulated patterns, suggesting the successful synthesis and high purity of these chains (Figures S5 and S6). Field emission scanning electron microscopy (SEM) characterization shows that their morphologies are long rod-shaped crystals, and the corresponding energy dispersive spectrometer (EDS) mapping proves the uniform distribution of elements such as Cu, N, Cl, Br, and I (Figure 1b–e). Thermogravimetric analysis (TGA) shows that structures of **Cu-PzCl**, **Cu-PzBr**, and **Cu-PzI** remain thermodynamically stable before heating to 280 °C. Compared to the other three chains, **Cu-PzH** lacks a platform due to without DMA solvent molecules in this structure (Figure S7). Moreover, these chains also have excellent chemical stability because the frameworks of these crystals remain intact after soaking in 1 M KOH for 3 days at room temperature (Figures S9 and S10). The CO_2 adsorption plots show that the adsorption capacity of **Cu-PzI** adsorption ability is slightly stronger than others (Figure S8). Based on the high thermodynamic and chemical stability of these four chains and their apparent CO_2 adsorption capacity, we believe that they may be suitable as electrocatalysts for CO_2 reduction.

The electrocatalytic activity and selectivity of these chain catalysts towards CO_2RR evaluate in a three-compartment flow cell employing the catalyst-modified carbon paper electrode as the working electrode and 1 M KOH as electrolyte. The performances of these electrodes are tested at a wide potential from −0.6 V to −1.1 V (vs. RHE) under a continuous flow of CO_2 (for faradic efficiencies using **Cu-PzX** as electrocatalysts, see the Supporting Information, Tables S2–55), While the gas and liquid products are analyzed by on-line gas chromatography (GC) and ^{1}H nuclear magnetic resonance spectroscopy (NMR) (Figures S11–S13). There is no liquid product detected by ^{1}H NMR (Figure S13). All the potentials are measured versus Ag/AgCl electrode, and the results were reported versus reversible hydrogen electrode (RHE).

During the electrocatalytic CO_2RR experiments, the polarization curves are performed by linear sweep voltammetry (LSV) mode at a scan rate of 8 mV s^{-1} in 1 M KOH solution with CO_2/Ar flowing in order to test the reaction activities of these chains. The current density of all these chains in the test voltage range (−0.6 to −1.1 V vs. RHE) in CO_2 atmosphere is higher than that in N_2 atmosphere, suggesting their higher reaction activity of electrocatalytic CO_2RR than HER (Figure 2b; Figure S14).

Based on the structural characteristics of the four chain catalysts, the influence of the coordination microenvironment on the selectivity of electrochemical CO_2RR products is systematically studied, the corresponding product distribution is displayed in Figure 2a. At the less negative potentials

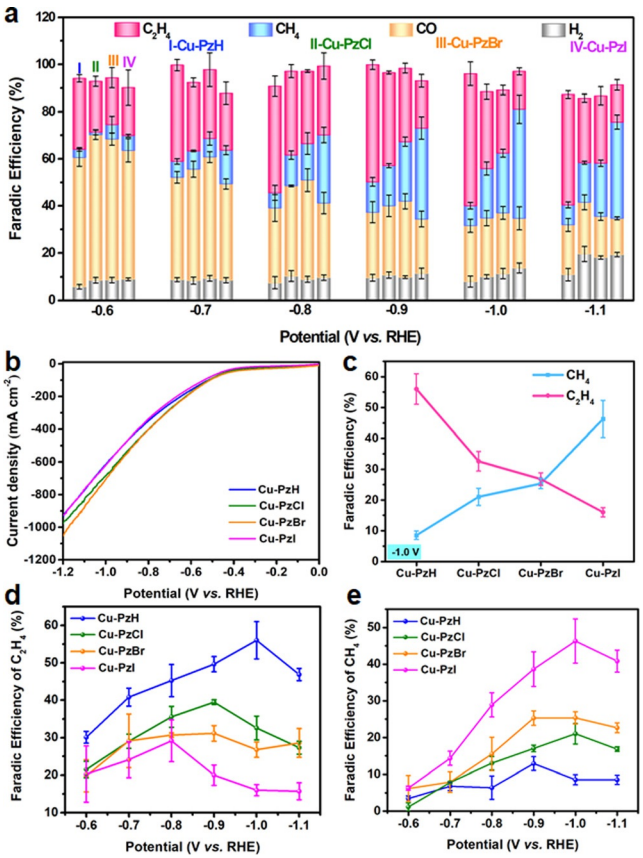

Figure 2. Electrocatalytic performance of Cu-PzX (where X = H, Cl, Br, I). a) All the faradic efficiency (FE) of products with **Cu-PzX** as electrocatalyst at different applied potentials (−0.6 V to −1.1 V). b) Linear sweep voltametric curves. c) FEs of CH_4 and C_2H_4 on **Cu-PzX** at −1.0 V. d) FEs for C_2H_4 on **Cu-PzX** at different applied potentials. e) FEs for CH_4 on **Cu-PzX** at different applied potentials.

(> −0.8 V), CO is determined to be the main reduction product ($FE_{CO} > 42\%$) for these chain catalysts, followed by C_2H_4. While we also detect CH_4 at initial potential, the amount is very low ($FE_{CH_4} < 14\%$). The main by-product is H_2 ($FE_{H_2} < 20\%$) formed by HER within the test voltage range (−0.6 to −1.1 V vs. RHE), which means that the designed single-chain model systems can effectively inhibit HER. Moreover, The FE_{CH_4} and $FE_{C_2H_4}$ increase with more negative potentials. For **Cu-PzH**, the $FE_{C_2H_4}$ continuously increases, and C_2H_4 is regarded as the dominant product; it gives the highest $FE_{C_2H_4}$ (60%) at −1.0 V with a large current density of −346.46 mA cm^{-2} along with 8.53% FE_{CH_4} and 23.57% FE_{CO}. This is the first case to achieve electrochemical CO_2RR to C_2H_4 with such high selectivity along with coordination polymer as the catalyst and shows one of the

best performances of electroreduction from CO_2 to CH_4 among Cu-based catalysts (Table S6). When the substituent of the 4-XPz ligand changes from Cl, Br to I atom, the FE of C_2H_4 gradually decreases, while the FE of CH_4 is increasing. For **Cu-PzCl** and **Cu-PzBr**, it gives the highest $FE_{C_2H_4}$ (39.4%, 31.14%) at −0.9 V and the highest FE_{CH_4} (21.03%, 25.35%) at −1.0 V (Figure 2d,e). Especially for **Cu-PzI**, the FE of CH_4 can rise up to 52% at −1.0 V with a large current density of $-287.52\ mA\,cm^{-2}$, and the FE of C_2H_4 drops to 16.04%. To further reveal the activity of the excellent performance of four chain catalysts, partial current densities of CH_4, CO, C_2H_4, and H_2 at different potentials are shown in Figures S15–S18. More importantly, it can be seen intuitively that the selective ratio of CH_4 and C_2H_4 gradually decreases from 1:6.5, 1:2.3, 1:1.2 to 1:0.3 at −1.0 V in flow cell (Figure 2c). In addition, we also calculate the mass productivities (weighted on copper mass) of C_2H_4 and CH_4 in **Cu-PzX** (Table S7). Besides, the bare carbon paper is measured as comparisons, and H_2 as the main product is detected (Figure S19). This result shows that the variation of coordination microenvironment in these chain catalysts indeed affects the selectivity of electrocatalytic products.

In order to verify the source of CH_4 and C_2H_4, the ^{13}C isotope labeling experiment is carried out by gas chromatography-mass spectrometry. As shown in Figure S20, the peak at $m/z = 29$, 17, 30 are, respectively assigned to ^{13}CO, $^{13}CH_4$, $^{13}C_2H_4$, indicating that the carbon source of the reduction products indeed derives from the CO_2 used. Besides, to further explore the potential factors of different product selectivity, the electrochemical double-layer capacitance (Cdl) measurements are carried out to estimate the electrochemical surface area (ECSA) (Figure S21). The results show that **Cu-PzI** indeed exhibits the largest Cdl value, and **Cu-PzH** exhibits the smallest Cdl value among four chains, which indicates that **Cu-PzI** can afford much more accessible active sites than the other chains. Meanwhile, the electrochemical impedance spectroscopy (EIS) measurement is carried out at the potential of −1.0 V vs. RHE to probe the electrocatalytic kinetics on the electrode/electrolyte surface (Figure S22). As revealed by the Nyquist plots, **Cu-PzI** has a much smaller charge transfer resistance, followed by **Cu-PzH**, proving that **Cu-PzI** enables to provide faster electron transfer from the catalyst surface to the reactant in the process of intermediate formation. Based on the above experimental results, it proves that **Cu-PzH** and **Cu-PzI** have different activity and selectivity for electrochemical CO_2RR. Notably, stability is a crucial criterion to evaluate the durability properties of catalysts for further applications. To analyze the electrochemical stability of these chain catalysts, the long-time durability tests of **Cu-PzH** and **Cu-PzI** as representative samples are assessed with chronoamperometric curves at −1.0 V. During the process, **Cu-PzH** shows the $FE_{C_2H_4}$ can be maintained higher than 50% with current density $\approx 340\ mA\,cm^{-2}$, and **Cu-PzI** shows the FE_{CH_4} can be maintained higher than 40% with current density $\approx 258\ mA\,cm^{-2}$ in continuous electrolysis throughout stability test. And we also calculate their TON for the long experiments (Table S8). By comparing the PXRD spectra before and after the test, it was found that the four chains could maintain their structure, which proved the stability of the catalyst (Figure S23).

Based on accurate crystalline structure models, the DFT calculation is carried out to further explain that the relationship between the coordination microenvironment variation and the performance differences in FE_{CH_4} and $FE_{C_2H_4}$ of these chain catalysts. In the process of CO_2 reduction, the change of the direct coordination microenvironment of catalytic active center usually has an important influence on its charge density distribution and electronic structure of Cu. Based on the above considerations, our DFT calculations mainly focus on the following two aspects. On one hand, as shown by the highest occupied molecular orbital (HOMO) and lowest unoccupied molecular orbital (LUMO) of these chains (Figure 3c), it's easy to find that the electron-donating ability of the HOMO is enhanced when the 4-XPz is gradually occupied by H, Cl, Br, and I. As an electric field is applied, the electrons on the HOMO are excited to the LUMO.[19] It is obvious that the charge density of different electronegative substituent atoms on the 4-XPz ligand is gradually moved to the Cu active center through the ligand, which corresponds to the charge transfer direction.

On the other hand, the partial densities of states (PDOS) of Cu active sites in these chain catalysts are performed to confirm the binding strength of the catalyst surface and the key reaction intermediate.[20] The Fermi level in calculation is set as 0 eV. When the 4-XPz is gradually occupied by H, Cl, Br, and I, it is obvious that the *d*-band center is upshifted from the Fermi energy level (E_f) due to the polarization of halogen, which increases from −3.22 eV in **Cu-PzH** to −3.01 eV in **Cu-PzI** (Figure 3a). In general, the closer the d-band center gets to the Fermi energy level, the more catalytic activity of Cu sites.[21] It leads to an increase in the binding strength of the metal active site and *HCO, which is difficult to further reducing the reaction barrier of the rate-determining step (RDS): *CO-*COH for generating C_2H_4. Therefore, it confirms the better selectivity of **Cu-PzI** for CH_4, which agrees with experimental results. However, **Cu-PzH** can only undergo C–C coupling and then hydrogenated because of its highest reaction barrier of RDS (*CO-*HCO), finally tends to produce C_2H_4. Moreover, as the *d*-band center gets closer to the Fermi level, **Cu-PzCl** and **Cu-PzBr** are in the transition state, witness that the adsorption ability of *HCO has changed from strong to weak, corresponding to the variation of selectivity trend from C_2H_4 to CH_4. These PDOS results verify that the upshift of the *d*-band center increases the adsorption energy of *HCO and affects the selectivity of the reduction product.

In order to further explore the important relationship of structure-performance that causes the difference in the electrocatalytic activity of the four chain catalysts, these chain structures are optimized (the Cu active sites have no coordination water molecules). The simulation results show that the synergistic effect ($D_{Cu\text{-}Cu}$ and $\beta_{Cu\text{-}Cu}$) between the neighboring bi-copper sites in these chains have apparent differences when the coordination microenvironment changes. The detailed structural parameters are shown in Figure 3b. For **Cu-PzH**, the $D_{Cu\text{-}Cu}$ shortens from 3.64 to 3.57 Å, meanwhile the $\beta_{Cu\text{-}Cu}$ increases from 71.67 to 74.48°,

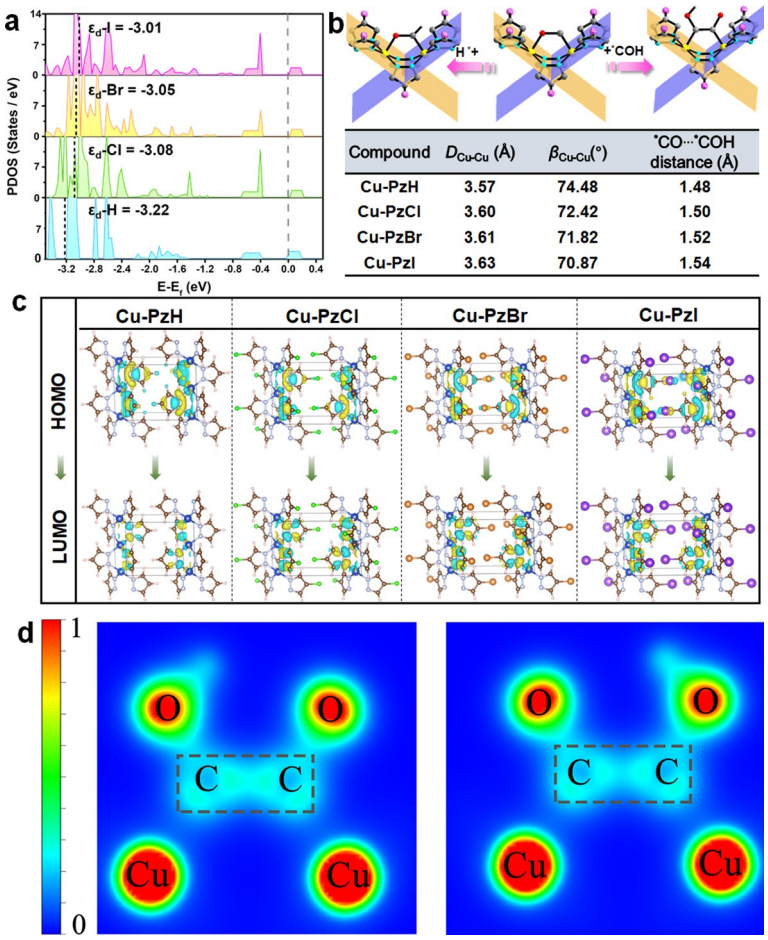

Figure 3. Exploring the potential relationship between structure and performance. a) Calculate the partial densities of states (PDOS) of Cu 3d for **Cu-PzX** (X = H, Cl, Br, I) catalysts. b) The important parameters (D_{Cu-Cu}, β_{Cu-Cu} and the distance of *CO···*COH for C–C coupling) and rate-determining step (RDS) in the optimized structure of **Cu-PzX** catalysts. c) Plots of charge density differences for **Cu-PzX** compounds. Blue and yellow areas indicate loss and gain of charge, respectively. d) 2D display of charge density of **Cu-PzH** (left) and **Cu-PzI** (right) systems, the electron-density isosurfaces are plotted at 0.15 e bohr^{-3}.

which cause the shortest *CO···*COH (1.48 Å) distance to realize the C–C coupling for generating C_2H_4 among these chains (Figure 3d). However, for **Cu-PzI**, the longest distance of *CO···*COH (1.54 Å) caused by the limitation of the D_{Cu-Cu} (3.63 Å) and the smallest β_{Cu-Cu} (70.87°) of adjacent bi-copper centers is not conducive to C–C coupling (Figure 3d). Therefore, the intermediate state of *CO is more inclined to hydrogenation for producing CH_4 in **Cu-PzI**. Additionally, the situation of the D_{Cu-Cu} and β_{Cu-Cu} of **Cu-PzCl** and **Cu-PzBr** are the same as PDOS trends. From **Cu-PzCl** to **Cu-PzBr**, the *CO···*COH distance gradually increases from 1.50 to 1.52 Å as a result of the D_{Cu-Cu} lengthening from 3.60 to 3.61 Å and the β_{Cu-Cu} decreasing from 72.42 to 71.82° in a small range, which also proves that C–C coupling is becoming more and more difficult. Thus, all the mentioned parameters, including Cu-Cu distance, dihedral angle, C–C distance, and orbital overlapping of CO* residues, are connected and all have influence on the C–C coupling ability.

Based on the results of experimental and theoretical calculations, we propose the possible electrochemical CO_2RR pathways for CO_2-to-CH_4 and CO_2-to-C_2H_4 conversions on these chain catalysts to better understanding the catalytic reaction mechanism (the detail free energy diagrams of CO_2 reduction to CO, CH_4, and C_2H_4 for **Cu-PzX** were shown at Figures S24–S27). As shown in Figure 4, the Gibbs free energy diagrams of reducing CO_2 to CH_4 and C_2H_4 illustrate their energy-favorable paths on these four chain catalysts at a potential of −1.0 V versus RHE, and provides the corresponding optimized structures of all intermediates generated on Cu active sites.[22] Obviously, the free energy change for the overall process was negative, which indicates that reducing CO_2 to CH_4 and C_2H_4 was thermodynamically favorable on the four chain catalysts. First, based on the lowest energy pathways for CH_4 generation, CO_2 is firstly converted from physical adsorption to chemical adsorption on two adjacent catalytic Cu sites and then quickly transformed into *COOH by hydrogenation. Subsequently, the *COOH is conformed into *CO intermediate by breaking the C–O bond.

Most importantly, the free energy calculations reveal that the step of *CO converted to *HCO determines the overall rate for CH_4 production. The Gibbs free energy (ΔG) value calculated at −1.0 V for *HCO formation on **Cu-PzI** is −0.15 eV, being lower than **Cu-PzH** (0.29 eV), **Cu-PzCl** (0.10 eV), and **Cu-PzBr** (0.007 eV), indicating that the reaction of *CO-*HCO is quite facile to occur on the **Cu-PzI** (Figure 4b). The proposed path carries on through in the sequence of *HCOH, *CH, *CH_2, *CH_3, CH_4(g) with the multi-step proton-electron transfer (Figure 4a). The detailed free energies for elementary steps involved in CH_4 generation from CO_2 reduction on **Cu-PzX** at −1.0 V are shown in Table S9.

However, based on the lowest energy pathways for C_2H_4 generation, the C–C coupling step (*CO-*COCOH) is recognized as the rate-determining step for CO_2RR to generate C_2H_4 on the **Cu-PzX**.[23] The detailed free energies for elementary steps involved in C_2H_4 generation from CO_2 reduction on **Cu-PzX** at −1.0 V are shown in Table S10. The reaction of *CO-*COCOH on **Cu-PzH**, **Cu-PzCl**, **Cu-PzBr**, and **Cu-PzI** with ΔG values of −0.49 eV, −0.09 eV, −0.05 eV, 0.10 eV, respectively (Figure 4d). Obviously, **Cu-PzH** is quite facile to carry out C–C coupling, leading to the highest selectivity to C_2H_4 formation, followed by **Cu-PzCl**, **Cu-PzBr**, and **Cu-PzI**. Particularly, the *COCOH species is considered as a key intermediate for C_{2+} product formation in CO_2RR. what's more, the *COC species is obtained by breaking the C–O bond of *COCOH, hydrogenating, and releasing water molecules. Then the *COCH, *COHCH, *CCH, *CHCH, *$CHCH_2$ intermediates generate by the multi-step proton-electron transfer processes. In the end, the produced C_2H_4 quickly desorbs from the catalyst surface. These steps are

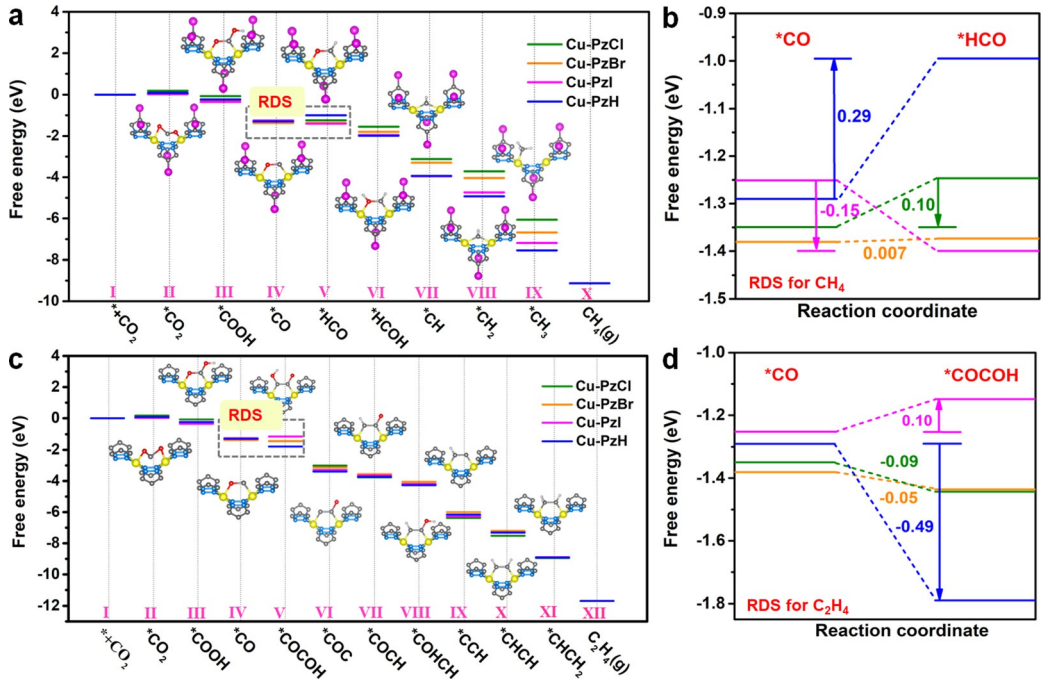

Figure 4. DFT calculations of reaction pathways on four catalysts models at a potential of −1.0V for CO_2RR. a) Free energy diagram of CO_2 reduction to CH_4 for **Cu-PzX** models, and optimized structures of all pathways involving reaction intermediates of CO_2RR to CH_4 on **Cu-PzI**. b) Comparing the corresponding ΔG of RDS (*CO-*HCO) for CH_4 in four chain catalysts. c) Free energy diagrams of CO_2 reduction to C_2H_4 for **Cu-PzX** models and optimized structures of all reaction intermediates involved in the pathways of CO_2RR to C_2H_4 on **Cu-PzH**. d) Comparing the corresponding ΔG of RDS (*CO-*COCOH) for C_2H_4 in four chain catalysts.

mainly downhill in free energy at −1.0 V, as shown in Figure 4c.

In short, the sequence of the reaction energies on four chain catalysts is well consistent with our experiments, which favorably support that the synergistic effect caused by coordination microenvironment variations of Cu active sites plays a critical role in the reaction mechanism and selectivity on specific reduction product. From our work, as the coordination microenvironment changes, the synergistic effect (the distance and dihedral angle) between the adjacent bi-copper active sites and the *d*-band center are also different. This fact makes two neighboring catalytic active sites have significant adsorption ability variations to intermediate species of different reduction products, which ultimately alters the electrocatalytic activation path and selectivity of the specific products.

Conclusion

In summary, we designed and synthesized crystalline single-chain models (**Cu-PzH**, **Cu-PzCl**, **Cu-PzBr**, and **Cu-PzI**) to explain CO_2 electroreduction product selectivity in a flow cell. The variation of coordination microenvironment changes the distances (from 3.57 to 3.63 Å) and dihedral angles (from 74.48 to 70.87°) between bi-copper atoms in these crystalline compounds, which directly leads to the selectivity of CH_4 and C_2H_4 showing a regular change from 1:6.5, 1: 2.3, 1:1.2 to 1:0.3. Specifically, **Cu-PzH** exhibits the highest $FE_{C_2H_4}$ (60%) at −1.0 V with a large current density of $-346.46\ mA\,cm^{-2}$. When the substituent of the 4-XPz ligand changes from Cl, to Br, and to I, the $FE_{C_2H_4}$ gradually decreases, while the FE_{CH_4} increases. **Cu-PzI** has the highest FE_{CH_4} of 52% at −1.0 V with a large current density of $-287.52\ mA\,cm^{-2}$. Based on experimental results and DFT calculations, the selectivity difference can be attributed to the following two key points. On one hand, the synergistic effect ($D_{Cu\text{-}Cu}$ and $\beta_{Cu\text{-}Cu}$) between neighboring catalytic active sites induced by the variation of the coordination microenvironment changes the distance of C–C coupling. On the other hand, the coordination microenvironment variation regulates the adsorption ability of the catalytically active center to the key reaction intermediates state by affecting the *d*-band center of copper. This work provides a stable and essential crystalline model system to study, systematically, the important influence of the coordination microenvironment variations of adjacent catalytic active centers on the activity and selectivity of C1 or C2 reduction products in CO_2RR.

Acknowledgements

This work is financially supported by the NSFC (No. 21622104, 92061101, 21871142 and 21901122); the NSF of Jiangsu Province of China (No. BK20171032); Natural Science Research of Jiangsu Higher Education Institutions of China (No. 19KJB150011) and Project funded by China Postdoctoral Science Foundation (No. 2018M630572 and 2019M651873) and the Priority Academic Program Development of Jiangsu Higher Education Institutions and the

Foundation of Jiangsu Collaborative Innovation Center of Biomedical Functional Materials.

Conflict of Interest

The authors declare no conflict of interest.

Keywords: copper · crystalline coordination compounds · single-chain model system · synergistic effects

[1] a) M. Ding, R. W. Flaig, H. L. Jiang, O. M. Yaghi, *Chem. Soc. Rev.* **2019**, *48*, 2783 – 2828; b) A. Vasileff, X. Zhi, C. Xu, L. Ge, Y. Jiao, Y. Zheng, S.-Z. Qiao, *ACS Catal.* **2019**, *9*, 9411 – 9417; c) O. S. Bushuyev, P. De Luna, C. T. Dinh, L. Tao, G. Saur, J. van de Lagemaat, S. O. Kelley, E. H. Sargent, *Joule* **2018**, *2*, 825 – 832.

[2] a) Y. Wang, Z. Chen, P. Han, Y. Du, Z. Gu, X. Xu, G. Zheng, *ACS Catal.* **2018**, *8*, 7113 – 7119; b) C.-T. Dinh, T. Burdyny, M. G. Kibria, A. Seifitokaldani, C. M. Gabardo, F. P. García de Arquer, A. Kiani, J. P. Edwards, P. De Luna, O. S. Bushuyev, C. Zou, R. Quintero-Bermudez, Y. Pang, D. Sinton, E. H. Sargent, *Science* **2018**, *360*, 783 – 787.

[3] a) S. Liu, H. Yang, X. Su, J. Ding, Q. Mao, Y. Huang, T. Zhang, B. Liu, *J. Energy Chem.* **2019**, *36*, 95 – 105; b) D. Gao, R. M. Arán-Ais, H. S. Jeon, B. Roldan Cuenya, *Nat. Catal.* **2019**, *2*, 198 – 210.

[4] A. Vasileff, C. Xu, Y. Jiao, Y. Zheng, S.-Z. Qiao, *Chem* **2018**, *4*, 1809 – 1831.

[5] a) T. Burdyny, W. A. Smith, *Energy Environ. Sci.* **2019**, *12*, 1442 – 1453; b) K. P. Kuhl, E. R. Cave, D. N. Abram, T. F. Jaramillo, *Energy Environ. Sci.* **2012**, *5*, 7050.

[6] a) J. J. Lv, M. Jouny, W. Luc, W. Zhu, J. J. Zhu, F. Jiao, *Adv. Mater.* **2018**, *30*, 1803111; b) A. S. Varela, *Curr. Opin. Green Sustainable Chem.* **2020**, *26*, 100371; c) A. S. Varela, M. Kroschel, T. Reier, P. Strasser, *Catal. Today* **2016**, *260*, 8 – 13.

[7] a) Y. Gao, Q. Wu, X. Liang, Z. Wang, Z. Zheng, P. Wang, Y. Liu, Y. Dai, M.-H. Whangbo, B. Huang, *Adv. Sci.* **2020**, *7*, 1902820; b) M. Song, D. Chen, Y. Yang, M. Xiang, Q. Zhu, H. Zhao, L. Ward, X.-B. Chen, *Adv. Funct. Mater.* **2021**, *31*, 2008028; c) G. L. De Gregorio, T. Burdyny, A. Loiudice, P. Iyengar, W. A. Smith, R. Buonsanti, *ACS Catal.* **2020**, *10*, 4854 – 4862.

[8] a) H.-Q. Liang, S. Zhao, X.-M. Hu, M. Ceccato, T. Skrydstrup, K. Daasbjerg, *ACS Catal.* **2021**, *11*, 958 – 966; b) R. Cao, J. D. Yi, R. Xie, Z. L. Xie, G. L. Chai, T. F. Liu, R. P. Chen, Y. B. Huang, *Angew. Chem. Int. Ed.* **2020**, *59*, 23641 – 23648; *Angew. Chem.* **2020**, *132*, 23849 – 23856; c) S. Chen, Y. Su, P. Deng, R. Qi, J. Zhu, J. Chen, Z. Wang, L. Zhou, X. Guo, B. Y. Xia, *ACS Catal.* **2020**, *10*, 4640 – 4646.

[9] R. Reske, H. Mistry, F. Behafarid, B. Roldan Cuenya, P. Strasser, *J. Am. Chem. Soc.* **2014**, *136*, 6978 – 6986.

[10] a) H. Mistry, A. S. Varela, C. S. Bonifacio, I. Zegkinoglou, I. Sinev, Y. W. Choi, K. Kisslinger, E. A. Stach, J. C. Yang, P. Strasser, B. R. Cuenya, *Nat. Commun.* **2016**, *7*, 12123; b) F. S. Roberts, K. P. Kuhl, A. Nilsson, *Angew. Chem. Int. Ed.* **2015**, *54*, 5179 – 5182; *Angew. Chem.* **2015**, *127*, 5268 – 5271; c) Y. Gu, J. Li, L. Wang, M. Xie, X. Wu, F. Xie, M. P. Ryan, *ChemistrySelect* **2019**, *4*, 10995 – 11001.

[11] a) T. T. H. Hoang, S. Verma, S. Ma, T. T. Fister, J. Timoshenko, A. I. Frenkel, P. J. A. Kenis, A. A. Gewirth, *J. Am. Chem. Soc.* **2018**, *140*, 5791 – 5797; b) J. Jiao, R. Lin, S. Liu, W. C. Cheong, C. Zhang, Z. Chen, Y. Pan, J. Tang, K. Wu, S. F. Hung, H. M. Chen, L. Zheng, Q. Lu, X. Yang, B. Xu, H. Xiao, J. Li, D. Wang, Q. Peng, C. Chen, Y. Li, *Nat. Chem.* **2019**, *11*, 222 – 228; c) X. Zheng, Y. Ji, J. Tang, J. Wang, B. Liu, H.-G. Steinrück, K. Lim, Y. Li, M. F. Toney, K. Chan, Y. Cui, *Nat. Catal.* **2019**, *2*, 55 – 61.

[12] P.-P. Yang, X.-L. Zhang, F.-Y. Gao, Y.-R. Zheng, Z.-Z. Niu, X. Yu, R. Liu, Z.-Z. Wu, S. Qin, L.-P. Chi, Y. Duan, T. Ma, X.-S. Zheng, J.-F. Zhu, H.-J. Wang, M.-R. Gao, S.-H. Yu, *J. Am. Chem. Soc.* **2020**, *142*, 6400 – 6408.

[13] Y. Zhou, F. Che, M. Liu, C. Zou, Z. Liang, P. De Luna, H. Yuan, J. Li, Z. Wang, H. Xie, H. Li, P. Chen, E. Bladt, R. Quintero-Bermudez, T. K. Sham, S. Bals, J. Hofkens, D. Sinton, G. Chen, E. H. Sargent, *Nat. Chem.* **2018**, *10*, 974 – 980.

[14] a) L. Sun, Z. Huang, V. Reddu, T. Su, A. C. Fisher, X. Wang, *Angew. Chem. Int. Ed.* **2020**, *59*, 17104 – 17109; *Angew. Chem.* **2020**, *132*, 17252 – 17257; b) J. Wang, X. Huang, S. Xi, H. Xu, X. Wang, *Angew. Chem. Int. Ed.* **2020**, *59*, 19162 – 19167; *Angew. Chem.* **2020**, *132*, 19324 – 19329; c) S. Dou, J. Song, S. Xi, Y. Du, J. Wang, Z. F. Huang, Z. J. Xu, X. Wang, *Angew. Chem. Int. Ed.* **2019**, *58*, 4041 – 4045; *Angew. Chem.* **2019**, *131*, 4081 – 4085.

[15] F. Li, A. Thevenon, A. Rosas-Hernandez, Z. Wang, Y. Li, C. M. Gabardo, A. Ozden, C. T. Dinh, J. Li, Y. Wang, J. P. Edwards, Y. Xu, C. McCallum, L. Tao, Z. Q. Liang, M. Luo, X. Wang, H. Li, C. P. O'Brien, C. S. Tan, D. H. Nam, R. Quintero-Bermudez, T. T. Zhuang, Y. C. Li, Z. Han, R. D. Britt, D. Sinton, T. Agapie, J. C. Peters, E. H. Sargent, *Nature* **2020**, *577*, 509 – 513.

[16] a) Y.-R. Wang, Q. Huang, C.-T. He, Y. Chen, J. Liu, F.-C. Shen, Y.-Q. Lan, *Nat. Commun.* **2018**, *9*, 4466; b) Z. Weng, J. Jiang, Y. Wu, Z. Wu, X. Guo, K. L. Materna, W. Liu, V. S. Batista, G. W. Brudvig, H. Wang, *J. Am. Chem. Soc.* **2016**, *138*, 8076 – 8079.

[17] a) W. Ma, S. Xie, T. Liu, Q. Fan, J. Ye, F. Sun, Z. Jiang, Q. Zhang, J. Cheng, Y. Wang, *Nat. Catal.* **2020**, *3*, 478; b) J. N. Lu, J. Liu, L. Z. Dong, S. L. Li, Y. H. Kan, Y. Q. Lan, *Chem. Eur. J.* **2019**, *25*, 15830 – 15836; c) Y.-C. Hsieh, S. D. Senanayake, Y. Zhang, W. Xu, D. E. Polyansky, *ACS Catal.* **2015**, *5*, 5349 – 5356.

[18] M. K. Ehlert, S. J. Rettig, A. Storr, R. C. Thompson, J. Trotter, *Can. J. Chem.* **1991**, *69*, 432 – 439.

[19] A. Beheshti, E. S. Mousavifard, S. Noorizadeh, P. Mayer, K. Woźniak, *Inorg. Chim. Acta* **2019**, *497*, 119082.

[20] Y. Pan, K. Sun, Y. Lin, X. Cao, Y. Cheng, S. Liu, L. Zeng, W.-C. Cheong, D. Zhao, K. Wu, Z. Liu, Y. Liu, D. Wang, Q. Peng, C. Chen, Y. Li, *Nano Energy* **2019**, *56*, 411 – 419.

[21] a) B. Hammer, J. K. Nørskov, *Surf. Sci.* **1995**, *343*, 211 – 220; b) B. Huang, L. Xiao, J. Lu, L. Zhuang, *Angew. Chem. Int. Ed.* **2016**, *55*, 6239 – 6243; *Angew. Chem.* **2016**, *128*, 6347 – 6351; c) Q. Li, Y. Ouyang, S. Lu, X. Bai, Y. Zhang, L. Shi, C. Ling, J. Wang, *Chem. Commun.* **2020**, *56*, 9937 – 9949.

[22] K. Zhao, X. Nie, H. Wang, S. Chen, X. Quan, H. Yu, W. Choi, G. Zhang, B. Kim, J. G. Chen, *Nat. Commun.* **2020**, *11*, 2455.

[23] H. Xiao, T. Cheng, W. A. Goddard 3rd, R. Sundararaman, *J. Am. Chem. Soc.* **2016**, *138*, 483 – 486.

Manuscript received: April 19, 2021
Revised manuscript received: June 19, 2021
Accepted manuscript online: June 23, 2021
Version of record online: July 28, 2021

